Reprinted from JOURNAL OF COMPUTATIONAL PHYSICS
All Rights Reserved by Academic Press, New York and London

Vol. 61, No. 2, November 1985
Printed in Belgium

Steady Viscous Flow Past a Circular Cylinder up to Reynolds Number 600*

BENGT FORNBERG

Exxon Research and Engineering Company, Annandale, New Jersey 08801

Received June 19, 1984; revised November 21, 1984

Viscous flow past a circular cylinder becomes unstable around Reynolds number $\mathrm{Re} = 40$. With a numerical technique based on Newton's method and made possible by the use of a supercomputer, steady (but unstable) solutions have been calculated up to $\mathrm{Re} = 600$. It is found that the wake bubble (region with recirculating flow) grows in length approximately linearly with Re. The width increases like $\mathrm{Re}^{1/2}$ up to $\mathrm{Re} = 300$ at which point a transition to linear increase with Re begins. At the highest Reynolds numbers we reached, the wake resembles a pair of translating, uniform vortices, both touching the center line. The cylinder, moving in front with the same speed, supplies the vorticity required to balance diffusion. © 1985 Academic Press, Inc.

INTRODUCTION

The structure of viscous steady flow past a circular cylinder at high Reynolds numbers forms one of the classical problems in fluid mechanics. In spite of much attention, several fundamental questions remain open. Apart from a previous calculation by the present author [6], complete, steady flow fields have been obtained numerically only up to $\mathrm{Re} = 120$. This is also close to the upper limit for experiments (due to temporal instabilities). Both numerics and experiments have pointed to a recirculation region growing in length like $O(\mathrm{Re})$ and in width like $O(\mathrm{Re}^{1/2})$. Persistence of these growth rates for $\mathrm{Re} \to \infty$ have been assumed in most recent asymptotic studies of steady high Reynolds number flows past a body (e.g., Smith [18, 19]). A possible Euler flow, consistent with this idea, was analyzed by Brodetsky [3] in 1923. It is known as the Helmholtz–Kirchhoff free streamline model. This suggested limit is characterized by two vortex sheets leaving the body tangentially approximately 55° from the upwind center line and extending to downstream infinity, enclosing a region of stagnant flow. Although this undoubtedly is a solution for $\mathrm{Re} = \infty$, Batchelor [2] gave, in 1956, several arguments suggesting this would be an unlikely limit for $\mathrm{Re} \to \infty$. He proposed an alternative

---

* Part of this study was performed while the author was working at the California Institute of Technology. It was then supported by Control Data Corporation, Department of Energy (Office of Basic Energy Sciences) and the John Simon Guggenheim Memorial Foundation.

0021-9991/85 $3.00

in which a finite wake with piecewise constant vorticity was bounded by vortex sheets. Only very few Euler solutions of this so called Prandtl–Batchelor type have been calculated (e.g., [17] contains one example and some further references). None of these are for flow past a cylinder. Even in cases where such Euler solutions exist, the question remains open whether they can be reached as limits for Re → ∞. Peregrine discusses in [12] some other possibilities for steady high Reynolds number wakes. Although he makes no firm predictions for Re → ∞, his arguments suggest (in agreement with our present results) that the width of the wake should be proportional to its length. In a recent study, Smith [20] also considers the possibility of wide wakes.

The calculation [6] showed a reversal of trends near Re = 300. Significant amounts of vorticity started to get convected into the interior of the recirculation region from behind. This caused the wake to grow wider and shorter. Our current work confirms the qualitative feature of vorticity recirculation from the end of the wake bubble and its rapid increase in width. However, the observed shortening of the wake is found to have been erroneous. The rate of increase for the width becomes nearly linear around Re = 450. In the remaining range of this calculation, i.e., up to Re = 600, a quite distinctive pattern emerges for the evolution of the flow. The wake consists mainly of a pair of vortices containing a low and very uniform level of vorticity. These vortex regions meet along the center line. They grow in size linearly with Re and follow a short distance behind the cylinder. The separated boundary layers from the body feed vorticity to the front edges of these regions, thus providing an influx of vorticity needed to balance diffusion. The region between the cylinder and these vortices has nearly zero interior vorticity.

All the numerical calculations in this present work were carried out on the Control Data Corporation Cyber 205 computers located at the CDC Service Centers in Arden Hills, Minnesota and in Rockville, Maryland. We wish to express our gratitude to Control Data Corporation for their extensive support of this study.

MATHEMATICAL FORMULATION

With a cylinder of radius 1 and a Reynolds number based on the diameter, the governing time independent Navier–Stokes equations, expressed in stream function Ψ and vorticity ω, take the form

$$\Delta\Psi + \omega = 0 \tag{1}$$

$$\Delta\omega + \frac{\mathrm{Re}}{2}\left\{\frac{\partial\Psi}{\partial x}\cdot\frac{\partial\omega}{\partial y} - \frac{\partial\Psi}{\partial y}\cdot\frac{\partial\omega}{\partial x}\right\} = 0. \tag{2}$$

Accurate numerical approximation and economical computational solution of these equations in the given geometry pose several difficulties which previous investigators have dealt with in a variety of ways. The most serious of the difficulties seem to be:

1. Boundary conditions for Ψ at large distances.
2. Boundary condition for ω at the body surface.
3. Avoiding the loss of accuracy that is associated with upwind differencing.
4. Economical choice of computational grid.
5. Reliable and fast rate of convergence of numerical iterations.

Point (5) above has been the limiting factor in virtually all previous attempts to reach high Reynolds numbers. No reliable technique has emerged to prevent slowly converging iteration schemes from picking up physical instabilities in the artificial time of the iterations.

NUMERICAL METHOD

All vorticity is concentrated on the body surface and in the wake downstream of the body. Outside this region the much simpler equations

$$\Delta\Psi = 0 \tag{3}$$

$$\omega = 0 \tag{4}$$

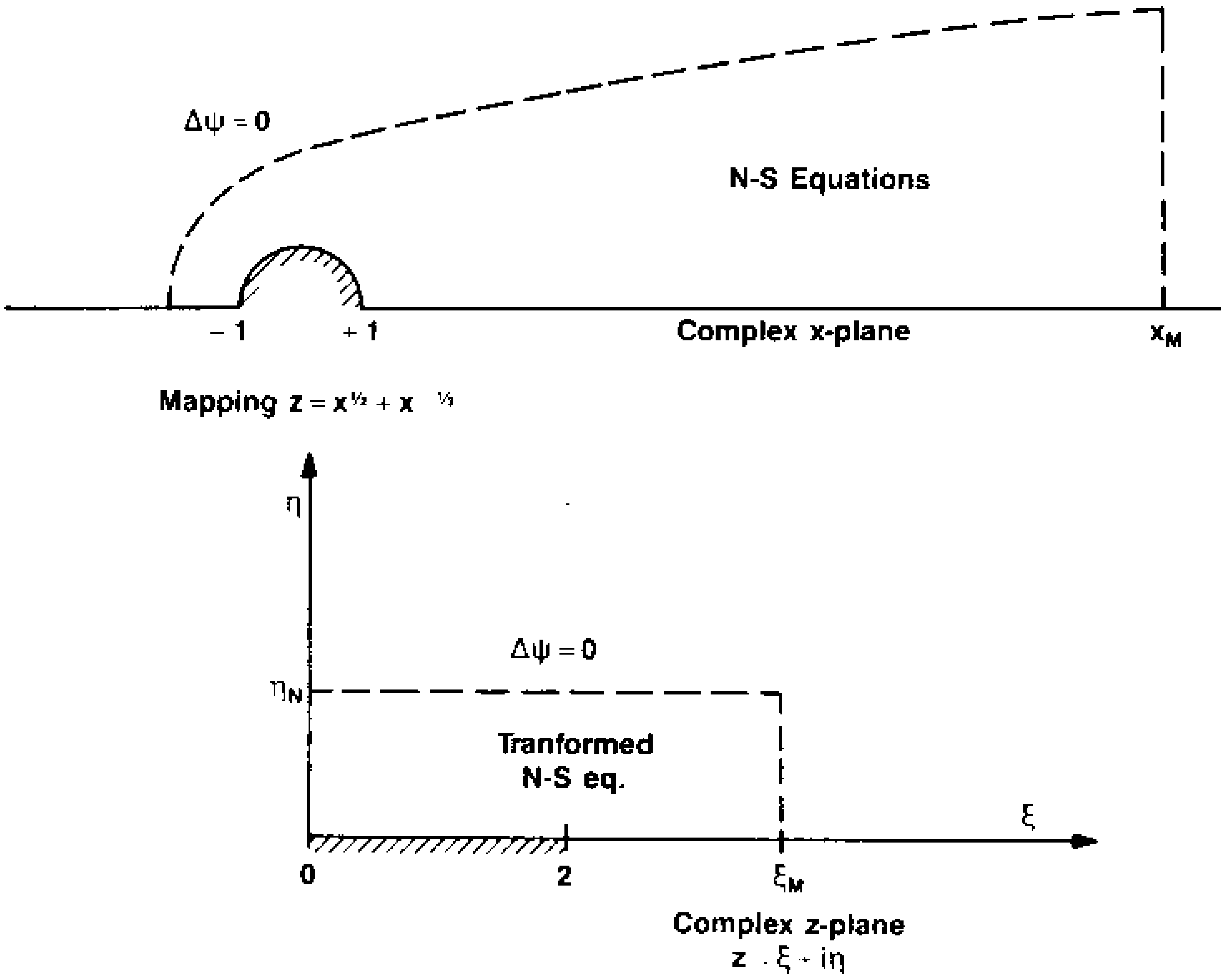

FIG. 1. Conformal mapping of the computational region.

are adequate. The top part of Fig. 1 shows the upper half plane minus a unit circle and, dotted, a region which contains all the vorticity (apart from the far wake). The bottom part of the figure shows how the mapping $z=\sqrt{x}+1/\sqrt{x}$ maps these two regions to the first quadrant and a rectangle, respectively. In all our calculations (apart from some designed only to test the accuracies of our boundary conditions) this rectangle was of size $\xi_M = 13\frac{1}{3}$ and $\eta_N = \frac{1888}{1215}$ (corresponding to a downstream cutoff at a distance of $x_M = 175.8$ radii from the cylinder).

Grids of three different densities were used. The "Fine Grid" had 541 * 109 points:

$$\begin{aligned} &\xi_i = 2i/81, \qquad i=0, 1,\ldots, 540, \\ &\eta_j = \alpha\zeta_j^3 + (1-4\alpha)\,\zeta_j, \qquad \zeta_j = 4j/243, \quad j=0, 1,\ldots, 108, \quad \alpha = 0.15. \end{aligned} \tag{5}$$

The two coarser grids contained 361 * 73 and 241 * 49 points (using $\xi_i = i/27$, $\zeta_j = 2j/81$ and $\xi_i = i/18$, $\zeta_j = j/27$, respectively). Thus, each coarser grid had $\frac{2}{3}$ as many points in each direction as the next finer one. Figure 2 illustrates the extent of the computational region and shows the coarsest of these three grids near the cylinder.

The Navier–Stokes equations, transformed to the z plane, take a form almost identical to (1) and (2):

$$\Delta\Psi + \omega/J = 0 \tag{6}$$

$$\Delta\omega + \frac{\mathrm{Re}}{2}\left\{\frac{\partial\Psi}{\partial\xi}\cdot\frac{\partial\omega}{\partial\eta} - \frac{\partial\Psi}{\partial\eta}\cdot\frac{\partial\omega}{\partial\xi}\right\} = 0 \tag{7}$$

where $J = |dz/dx|^2$ is the Jacobian of the mapping. These equations were modified further by subtracting out potential flow. The stream function ψ for the difference is

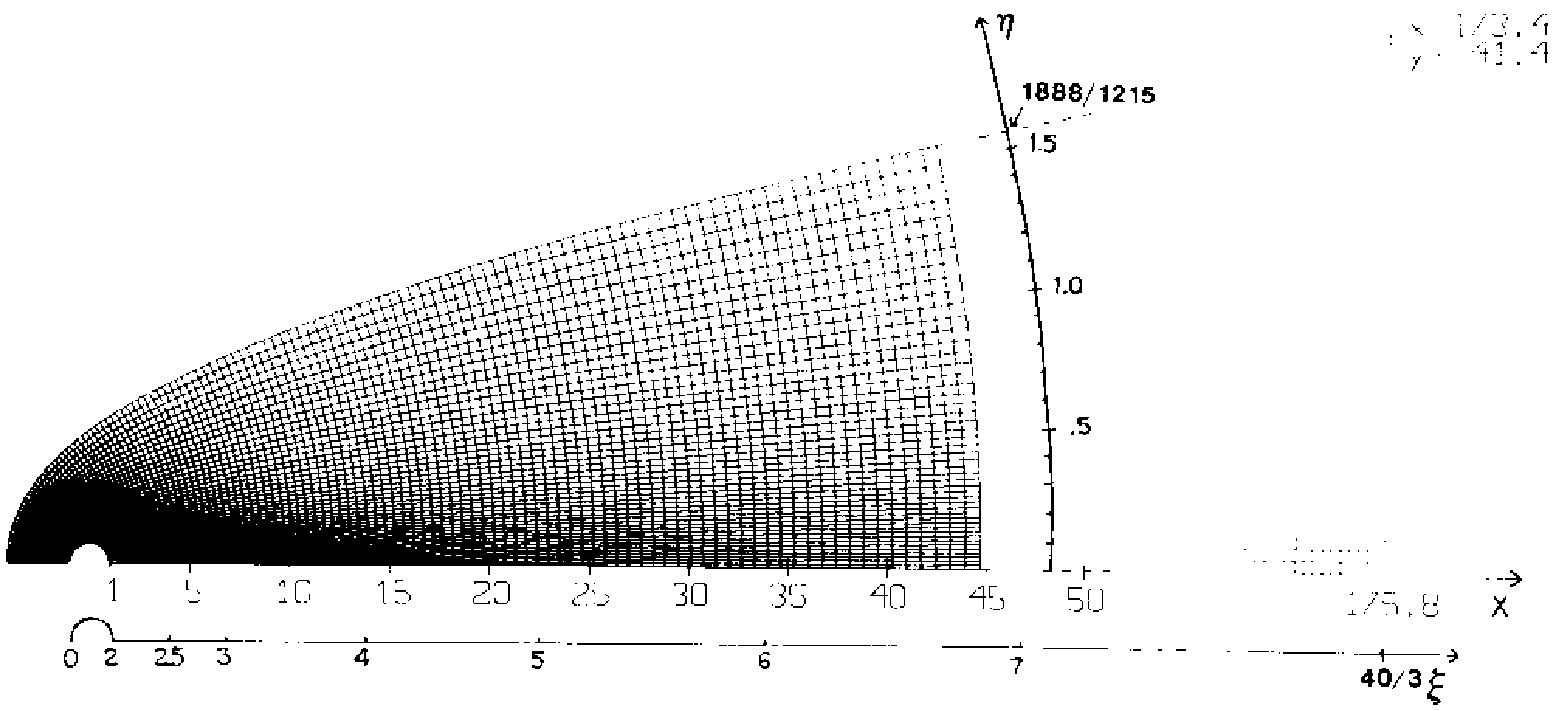

FIG. 2. Part near the cylinder of the 241*49 grid.

$\psi = \Psi - 2\xi\eta$. On a grid in the (stretched) z plane, Eqs. (6) and (7) were approximated at all interior points with centered second-order finite differences. To close the system, boundary conditions have to be implemented for ψ and ω.

The extreme sensitivity of the final solution to small errors in these conditions has only recently been fully recognized [6]. Already at Re = 2 it was found that use of the free stream value for ψ along circular outer boundaries at distances 23.1 and 91.5 caused 18% and 4.4% errors in the level of vorticity on the body surface.

The "Oseen" approximation is the leading term in an asymptotic expansion for the flow far out in a wake (e.g., Imai [9]). In polar coordinates, it takes the form

$$\psi = \frac{C_D}{2}\left(\frac{\theta}{\pi} - \operatorname{erf} Q\right) \tag{8}$$

$$\omega = -\frac{C_D \operatorname{Re} Q}{4\sqrt{\pi}\, r} e^{-Q^2} \tag{9}$$

where $Q = (\frac{1}{2} \operatorname{Re} r)^{1/2} \sin \frac{1}{2}\theta$, $\operatorname{erf} Q = 2\pi^{-1/2} \int_0^Q e^{-s^2}\, ds$ and C_D the drag coefficient. C_D can be evaluated as a line integral around the body.

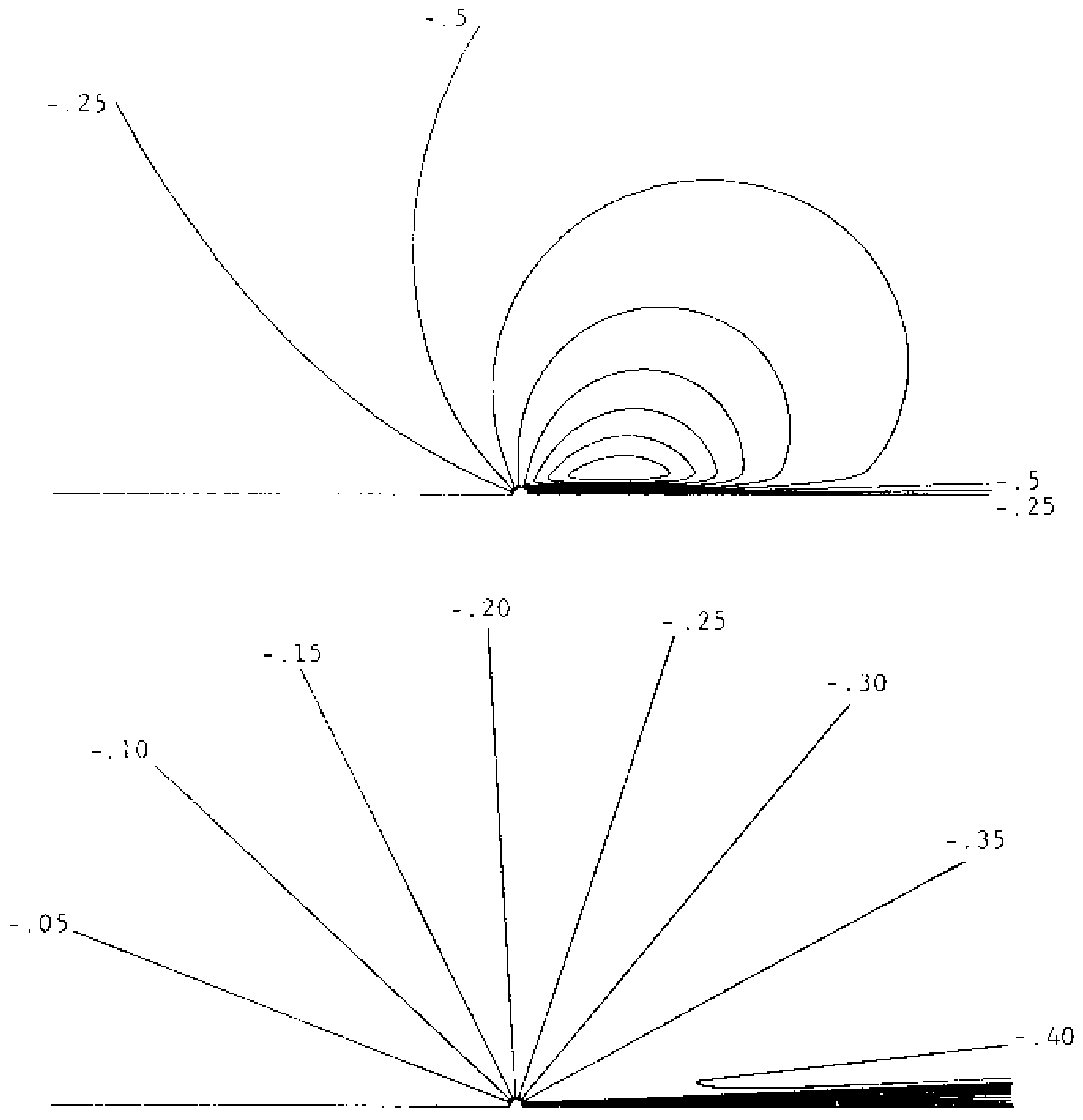

FIG. 3. Difference between streamfunction and free stream compared with the Oseen approximation for Re = 200.

The performance of this Oseen condition as an outer boundary condition proves to be disappointing. The percentage errors mentioned above improve, but only to 3.4 and 1.2%, respectively. For increasing Re, direct use of (8) becomes meaningless. Figure 3 illustrates this by comparing the true ψ (here the difference between streamfunction and free stream, not potential flow) with the values from (8) at Re = 200. The two fields bear no resemblance to each other at the distances from the body we are interested in. (Further terms in the Oseen expansion do not significantly effect this discrepancy.)

Comparison with numerics suggests that (9) is far more accurate than (8). Furthermore

1. Any errors in (9) are present only in a very narrow region along the outflow axis, not along the whole upper boundary as with (8).
2. The governing equation for ω is of a type which cannot transport incorrect information for ω back up towards the cylinder.

With this background, let us briefly outline how the boundary conditions of high accuracy can be implemented on the edges of the present computational region.

Boundary Conditions for ω

Left boundary:	$\xi = 0, 0 \leqslant \eta \leqslant \eta_N$;	$\omega = 0$.
Bottom boundary:	$\eta = 0, 0 \leqslant \xi < 2$;	a relation based on $\Delta\psi + \omega/J = 0$, ψ an even function of η;
	$2 \leqslant \xi < \xi_M$;	$\omega = 0$.
Right boundary:	$\xi = \xi_M, 0 \leqslant \eta < \eta_N$;	$\omega_{\xi_M} = \omega_{\xi_{M-1}}(\xi_{M-1}/\xi_M)^2$.
Top boundary:	$\eta = \eta_N, 0 \leqslant \xi \leqslant \xi_M$;	$\omega = 0$.

The condition at the right boundary comes from the observation that the leading term of (9), transformed to ξ, η-coordinates simplifies to

$$\omega = \frac{c_1}{\xi^2} e^{-c_2 \eta}, \tag{10}$$

where c_1 and c_2 are constants. The mapping has achieved a separation of variables.

Boundary Conditions for ψ

Left boundary:	$\xi = 0, 0 \leqslant \eta \leqslant \eta_N$;	$\psi = 0$.
Bottom boundary:	$\eta = 0, 0 \leqslant \xi \leqslant \xi_M$;	$\psi = 0$.
Right boundary:	$\xi = \xi_M, 0 \leqslant \eta < \eta_N$;	$\partial^2\psi/\partial\eta^2 = \omega$ (noting that $\partial^2\psi/\partial\xi^2 \ll \partial^2\psi/\partial\eta^2$ along this boundary).
Top boundary:	$\eta = \eta_N, 0 \leqslant \xi \leqslant \xi_M$;	A finite difference scheme connecting ψ-values on the top two grid levels as described below.

Boundary conditions which simulate the asymptotic decay of solutions in infinite regions have been derived independently several times for special applications (e.g., [5, 6]). More general discussions on this subject can be found in [8, 11]. We propose here a method which, for Laplace's equation, gives a convenient finite difference formulation.

The difference formula we are looking for should be satisfied by all modes which decay for η increasing but reject all modes which grow. We consider the Cauchy problem for $\Delta\psi = 0$ and discretize it only in the ξ-direction with $\xi_k = k \cdot \Delta\xi$, $k = ..., -2, -1, 0, 1, 2,...$:

$$\frac{\partial^2\psi(\xi,\eta)}{\partial\eta^2} - \frac{\psi(\xi-\Delta\xi,\eta) - 2\psi(\xi,\eta) + \psi(\xi+\Delta\xi,\eta)}{\Delta\xi^2} = 0 \tag{11}$$

A δ-function initial condition $\psi(\xi,\eta) = \delta(k)$ contains equal amounts of all Fourier modes. Each mode can either grow or decay for η increasing. Choosing the decaying mode, Fourier recomposition at level $\eta + \Delta\eta$ gives

$$\psi(\xi_k, \eta + \Delta\eta) = \frac{1}{2\pi}\int_0^{2\pi} e^{-2\lambda \sin(z/2)} \cos kz\, dz = c_k(\lambda), \tag{12}$$

where $\lambda = \Delta\eta/\Delta\xi$. The finite difference stencil,

$$\begin{array}{lccccccc} \text{level } \eta+\Delta\eta & & & & 1 & & & \\ \text{level } \eta & \cdots & -c_2(\lambda) & -c_1(\lambda) & -c_0(\lambda) & -c_1(\lambda) & -c_2(\lambda) & \cdots, \end{array}$$

gives a relation for ψ between the two top grid lines. The further condition that $\psi = 0$ along $\xi = 0$ may be taken into account by a simple modification of the coefficients. The right-hand truncation at a finite $\xi = \xi_M$ can be approximated by assigning $\psi(\xi,\eta) = \psi(\xi_M, \eta)$ for $\xi > \xi_M$.

In our calculations, we have chosen to use a slightly more symmetric version of this difference formula, namely

$$\begin{array}{lcccccc} \text{level } \eta+\Delta\eta & \cdots c_2\left(-\frac{\lambda}{2}\right) & c_1\left(-\frac{\lambda}{2}\right) & c_0\left(-\frac{\lambda}{2}\right) & c_1\left(-\frac{\lambda}{2}\right) & c_2\left(-\frac{\lambda}{2}\right) \cdots, \\ \text{level } \eta & \cdots -c_2\left(\frac{\lambda}{2}\right) & -c_1\left(\frac{\lambda}{2}\right) & -c_0\left(\frac{\lambda}{2}\right) & -c_1\left(\frac{\lambda}{2}\right) & -c_2\left(\frac{\lambda}{2}\right) \cdots, \end{array}$$

again suitably modified to include the end effects.

The coefficients $c_k(\lambda)$, $k = 0, 1, 2,...$, can be calculated directly from (12). For increasing values of k, the following asymptotic expansion becomes useful:

$$\begin{aligned}\pi c_k(\lambda) &= \frac{1}{k^2}(\lambda) + \frac{1}{k^4}\left(\frac{\lambda}{4} - \lambda^3\right) + \frac{1}{k^6}\left(\frac{\lambda}{16} - \frac{5}{2}\lambda^3 + \lambda^5\right)\\ &+ \frac{1}{k^8}\left(\frac{\lambda}{64} - \frac{91}{16}\lambda^3 + \frac{35}{4}\lambda^5 - \lambda^7\right)\\ &+ \frac{1}{k^{10}}\left(\frac{\lambda}{256} - \frac{205}{16}\lambda^3 + \frac{483}{8}\lambda^5 - 21\lambda^7 + \lambda^9\right)\\ &+ \frac{1}{k^{12}}\left(\frac{\lambda}{1024} - \frac{7381}{256}\lambda^3 + \frac{12485}{32}\lambda^5 - \frac{2541}{8}\lambda^7 + \frac{165}{4}\lambda^9 - \lambda^{11}\right) + \cdots.\end{aligned} \tag{13}$$

The discrete approximations at the interior points together with the boundary conditions form, after minor simplifications (explicitly eliminating all boundary unknowns apart from ψ at the top boundary), a non-linear algebraic system of $(M-2)(2N-3)$ equations with equally many unknowns. In most earlier works, great care has been taken to ensure that, at this stage, this (or some equivalent) non-linear system has a diagonally dominant form for low Re. This would allow direct functional iteration to convergence. Techniques such as upwind differencing [1, 4, 14] help in this respect at the cost of lowered accuracy. Newton's method, described below, offers an outstanding alternative.

NEWTON'S METHOD

Newton's method is a well-known procedure for finding zeros of non-linear systems of equations. Each iteration involves the solution of a linear system. Convergence is quadratic and guaranteed to occur for approximations sufficiently close to any "simple" solution. The realization that this procedure is practical for extremely large systems (several tens of thousands of equations) is rather recent and linked to the emergence of powerful computers.

For our present problem, use of Newton's method offers several major advantages:

1. The quadratic convergence rules out all possibilities of physical instabilities in real time being carried over to the artificial time of the iterations. Convergence is guaranteed if an isolated solution exists in the neighborhood of an initial approximation.

2. If turning points or bifurcation points are found, they will cause no serious difficulties.

3. No upwind differencing is needed. This procedure is typically employed for two reasons: (1) to ensure convergence of an iterative method; (2) to avoid mesh size oscillations. The first reason no longer applies. Our outflow boundary condition for ω proved very effective in suppressing potential oscillations.

4. Boundary conditions at the body surface become easier to implement. The fact that we have two conditions for ψ and none for ω can cause a problem if (6) and (7) are treated separately. With Newton's method it is sufficient that the conditions are independent and their number is right.

The main disadvantage with Newton's method is a rather high computational cost.

SOLUTION OF LINEAR SYSTEM

For a grid with $M*N$ points, we introduce the vectors $\psi_1, \psi_2, ..., \psi_{M-1}$, and ψ_{N-1} of lengths $N-2$ and $M-1$ elements, respectively. They denote the unknown ψ-values at grid points not on the coordinate axis (see Fig. 4). For the ω-values, we similarly introduce $\omega_1, ..., \omega_{M-1}$ ($\omega_{N-1} = 0$ and not unknown). With this ordering of the unknowns and a matching ordering of the equations, Fig. 5 shows the Jacobian in Newton's method. Since the top right corner contains a single diagonal, explicit multiples of the top $(N-2)(M-2)$ equations can be superposed on the equations below to eliminate the bottom right corner. The bottom left corner forms a separated system of size $(N-1)(M-2)$ with a structure shown in Fig. 6 (the specific dimensions given in the figure correspond to the "Fine Grid" with $M = 541$, $N = 109$). This system was solved by a border algorithm similar to the one described in [10]. The code was written with particular attention being paid to minimize the number of page faults in the virtual memory of the Cyber 205 computer (no explicit I/O was performed to accomodate the arrays of approximately 60 M words required during the solution).

The complete linear solver lends itself very well to vectorization. Every part of significant cost turns out to take the form of a "linked triad" with vectors never shorter than $4(N-2)+1$ or $M-2$. The linked triad is the fastest floating point operation on the Cyber 205. Expressions of the form vector–op–vector–op–scalar, where one "op" is + or −, the other * can execute with both operations running

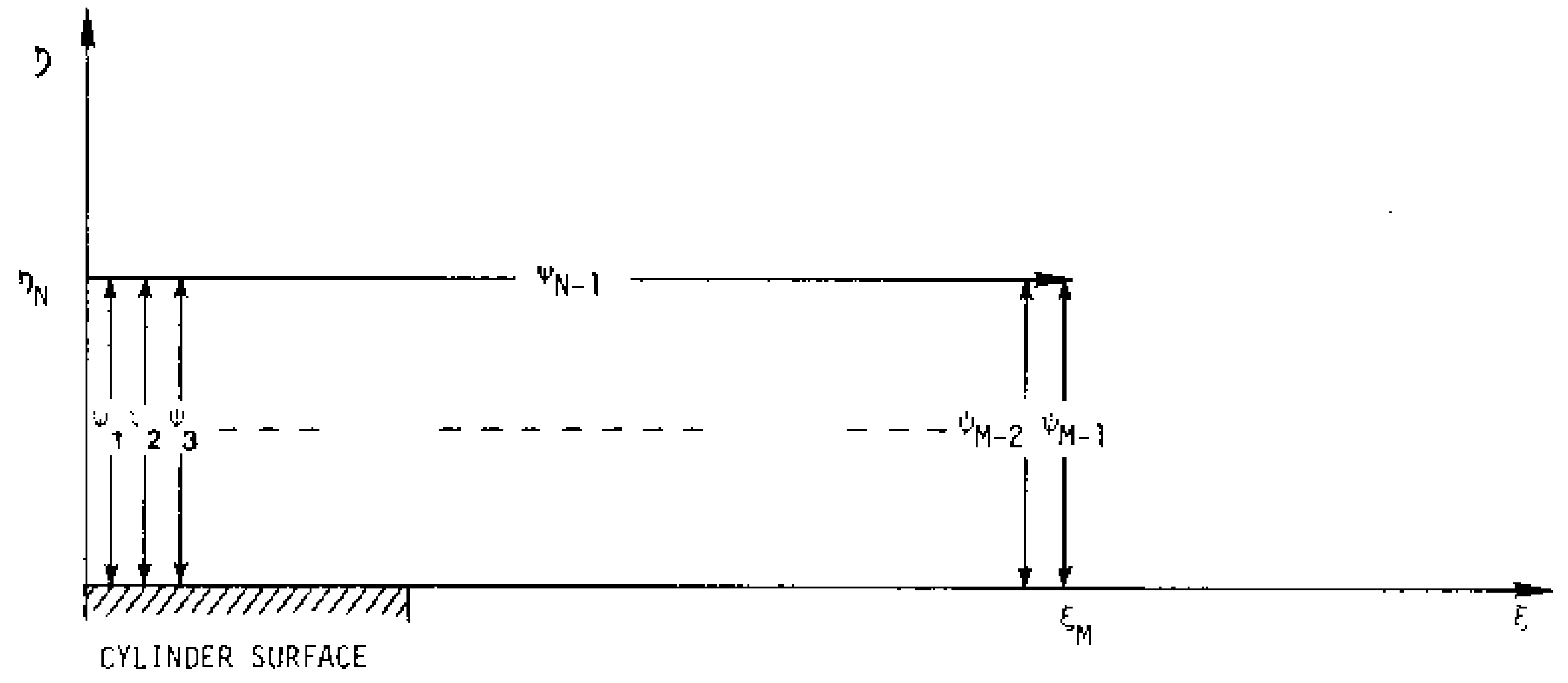

FIG. 4. Notation for the vectors of unknowns.

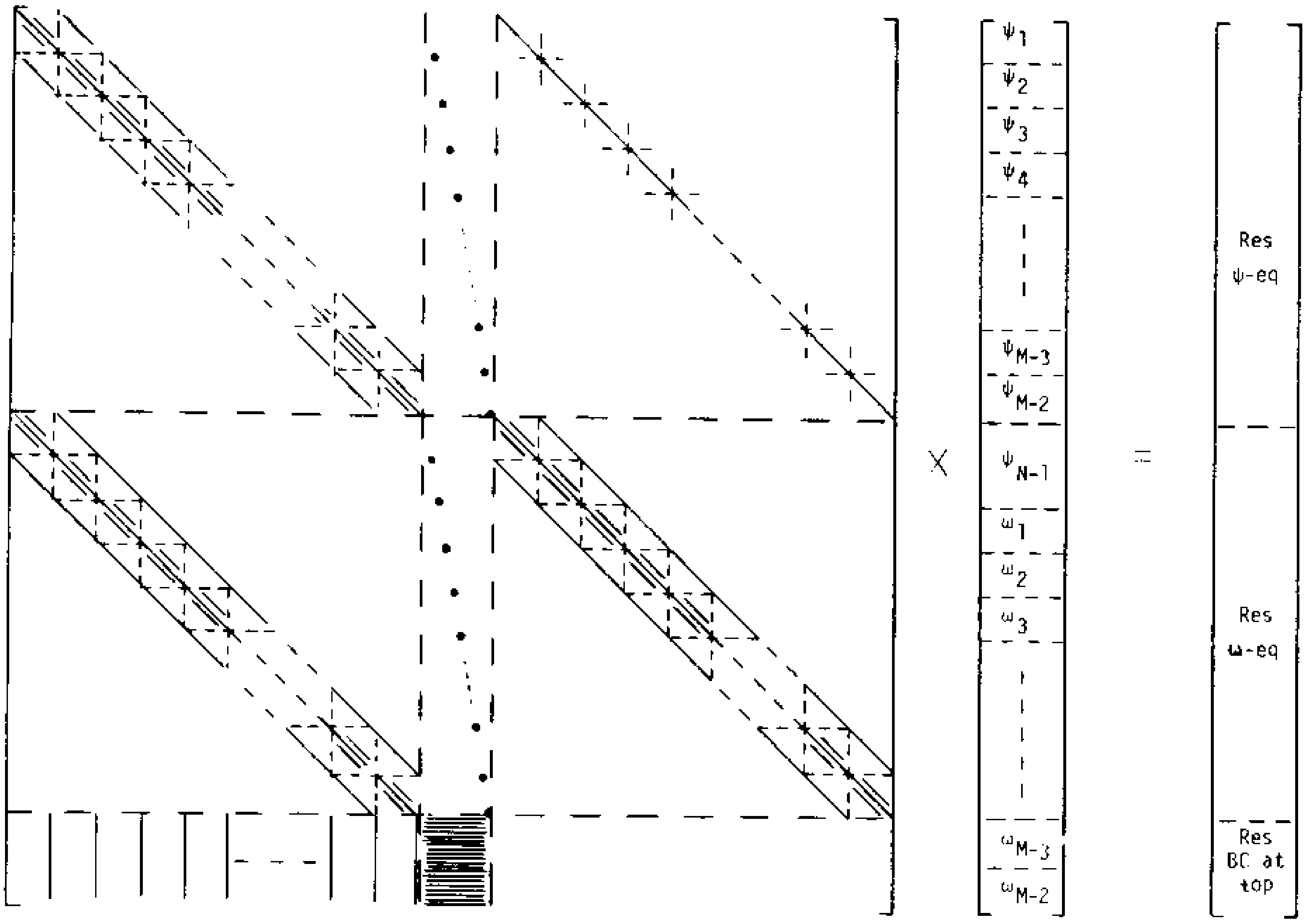

FIG. 5. Structure of the linear system in Newton's method.

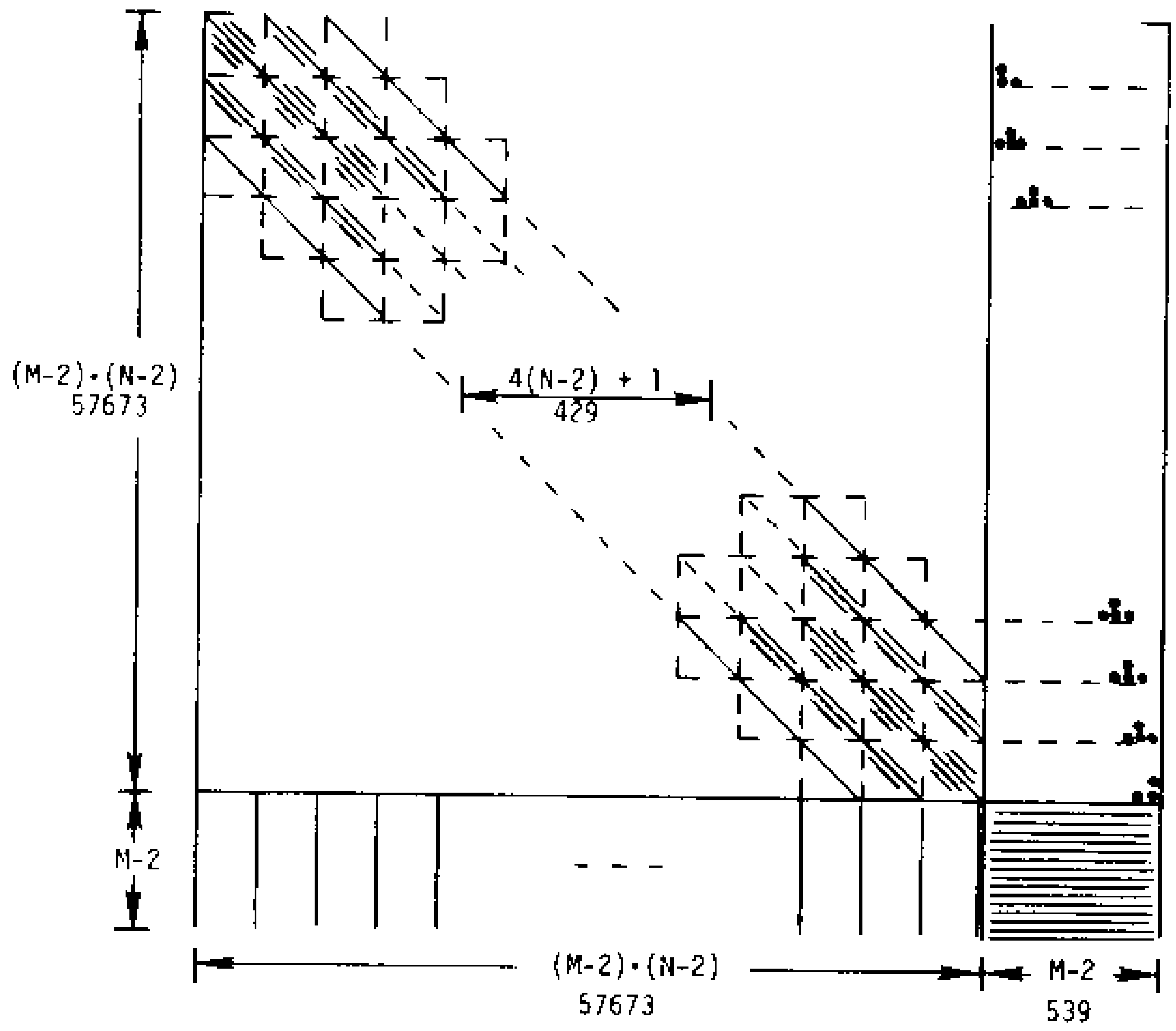

FIG. 6. Structure of the reduced Jacobian.

simultaneously. For a 2-pipe Cyber 205, the peak speed is 200 Mflops (million floating point operations per second, 64-bit accuracy). Due to scalar overhead, frequent page faults and limited vector lengths (averaging around 400), the actual measured computational rates were significantly lower. For our fine grid, the setup time for each Jacobian was 0.040 s and the solution time for each linear system (requiring $5.1*10^{10}$ arithmetic operations) was 403 s. This gives a sustained average speed of 127 Mflops.

NUMERICAL RESULTS

Figures 7 and 8 show contour lines for the streamfunction and the vorticity for different Reynolds numbers up to 600. Figure 9 illustrates the vorticity distribution

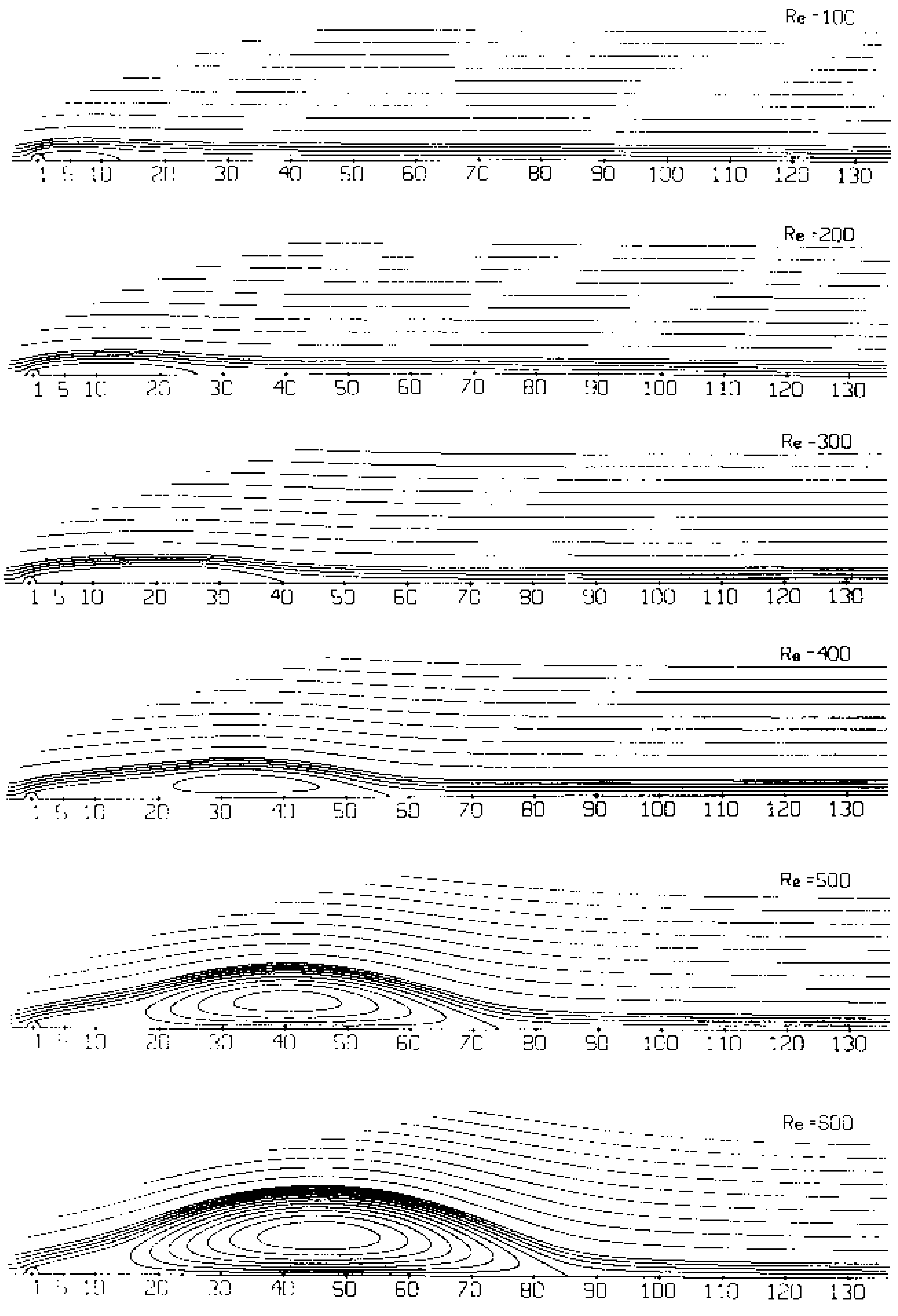

FIG. 7. Streamlines.

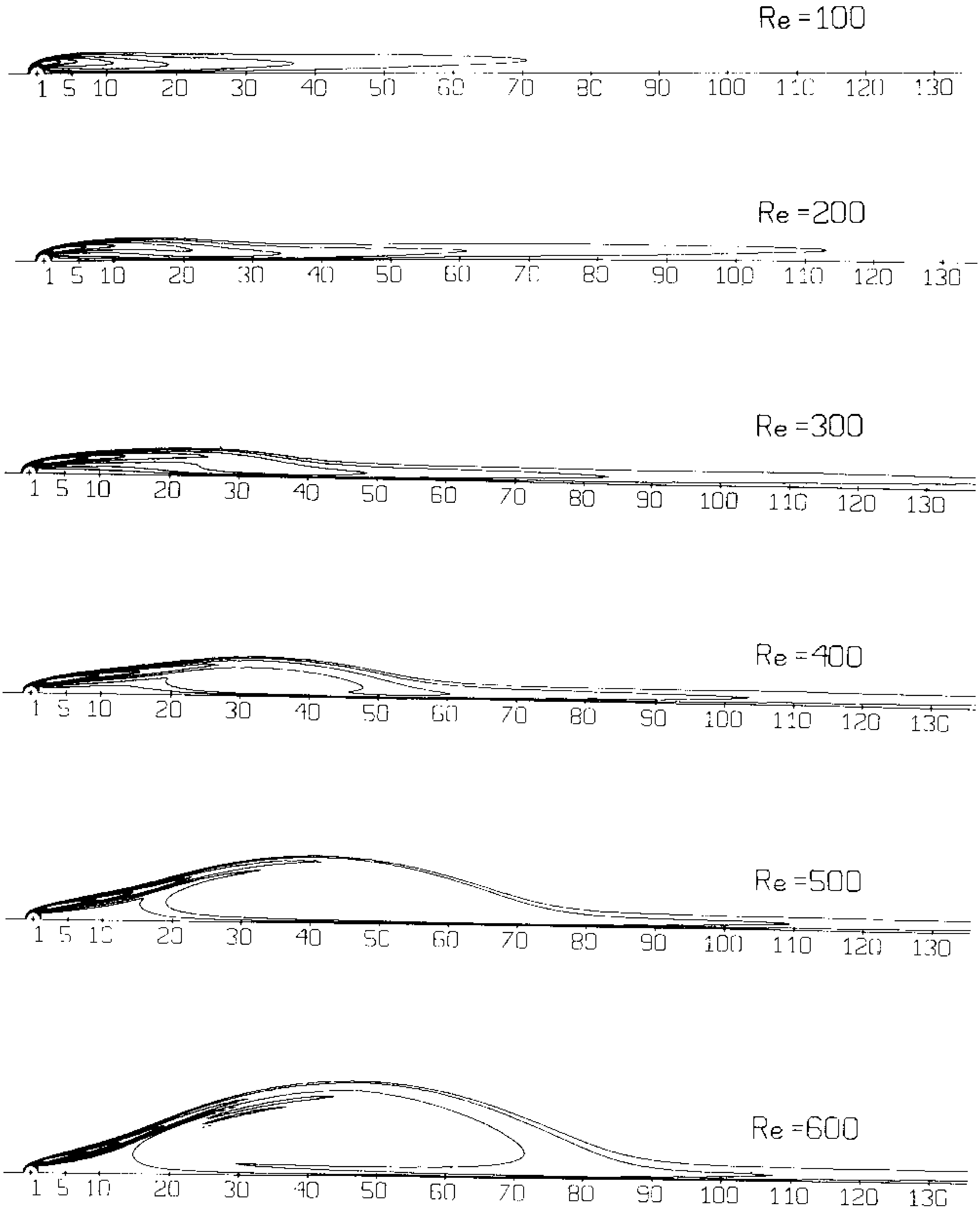

FIG. 8. Contours of constant vorticity.

in a different way (note that the widths of the wakes appear exaggerated in this figure because of different scales in the x and y directions). Starting around $\mathrm{Re}=300$, the vorticity fields show a recirculation back into the wake from the end of the bubble. With this is associated a quite sudden increase in width. At approximately $\mathrm{Re}=500$, this increase in width seems to have settled to a linear rate. The linear growth in length is unaffected by this transition around $\mathrm{Re}=300$. For Reynolds numbers 400, 500, and 600, Fig. 9 shows distinct interior plateaus of constant vorticity. The levels in these three cases are -0.333, -0.241, and -0.198, respectively. (The few erroneous contours near the top of the bubble in Fig. 8, $\mathrm{Re}=600$ appeared because the plateau value of -0.198 happened to be very close to -0.2 which was used as one of the contour levels.)

Figures 10 and 11 show the results we have obtained for the length and maximum width of the wake bubble with use of the three different grid densities. Only for the results in Figs. 7–11 were any noticeable differences present between the two finer grids. In these cases, the "Fine Grid" was used at Re 500 and 600. The remaining figures are based on the "Medium Grid" ($M=361$, $N=73$) at all Reynolds numbers. Figure 12 shows the vorticity along the body surface as a function of the polar coordinate angle, measured from the front stagnation point. We note that the magnitude of the surface vorticity decreases with increasing Re at the upper end of this calculation.

With our definition of Re, the pressure p satisfies the following equations in the physical x-y coordinate system:

$$\frac{\partial p}{\partial x}=-\frac{2}{\mathrm{Re}}\omega_y+\Psi_x\Psi_{yy}-\Psi_y\Psi_{xy} \tag{14}$$

$$\frac{\partial p}{\partial y}=\frac{2}{\mathrm{Re}}\omega_x+\Psi_y\Psi_{xx}-\Psi_x\Psi_{xy}. \tag{15}$$

Changing notation to let x denote complex positions in the x plane, an arbitrary conformal mapping $z=z(x)$, where $z=\xi+i\eta$ transforms (14) and (15) into

$$\frac{\partial p}{\partial \xi}=-\frac{2}{\mathrm{Re}}\omega_\eta+|g(x)|(\Psi_\xi\Psi_{\eta\eta}-\Psi_\eta\Psi_{\xi\eta})-\mathrm{Real}\,h(x)(\Psi_\xi^2+\Psi_\eta^2) \tag{16}$$

$$\frac{\partial p}{\partial \eta}=\frac{2}{\mathrm{Re}}\omega_\xi+|g(x)|(\Psi_\eta\Psi_{\xi\xi}-\Psi_\xi\Psi_{\xi\eta})-\mathrm{Im}\,h(x)(\Psi_\xi^2+\Psi_\eta^2), \tag{17}$$

where $g(x)=(dz/dx)^2$ and $h(x)=\overline{(d^2z/dx^2)}(g(x)/|g(x)|)$. Following the integration paths illustrated in Fig. 13a, the pressure was calculated at all grid points. The computational domain does not reach sufficiently far out in any direction to allow a firm normalization of $p=0$ at infinity. As an approximation, we have set $p=0$ at the top right corner of the grid (with physical coordinates (173.4, 41.4)). Figure 13b shows a different path, also connecting this corner to the front stagnation point.

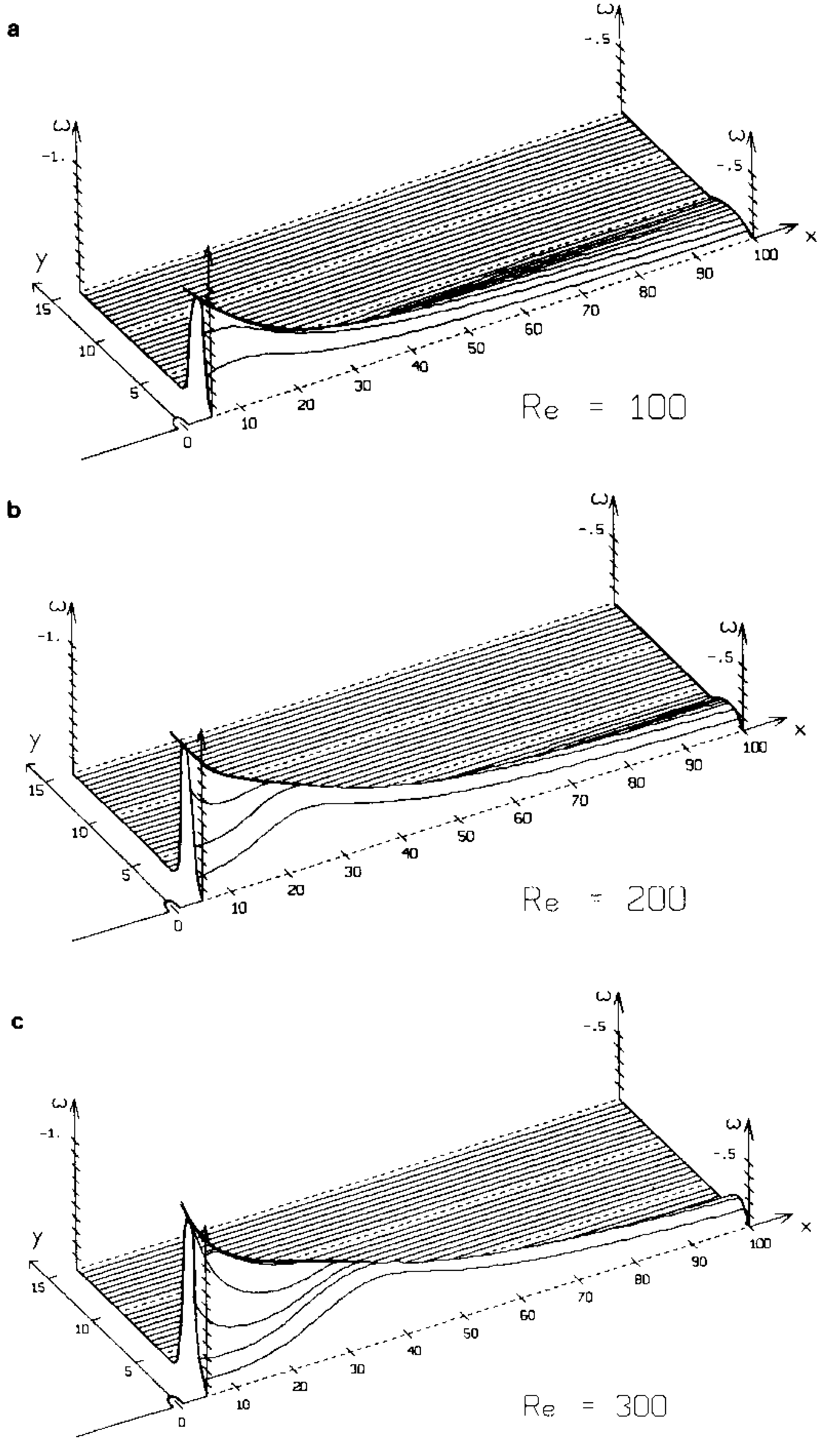

FIG. 9. Distribution of vorticity in wake behind cylinder.

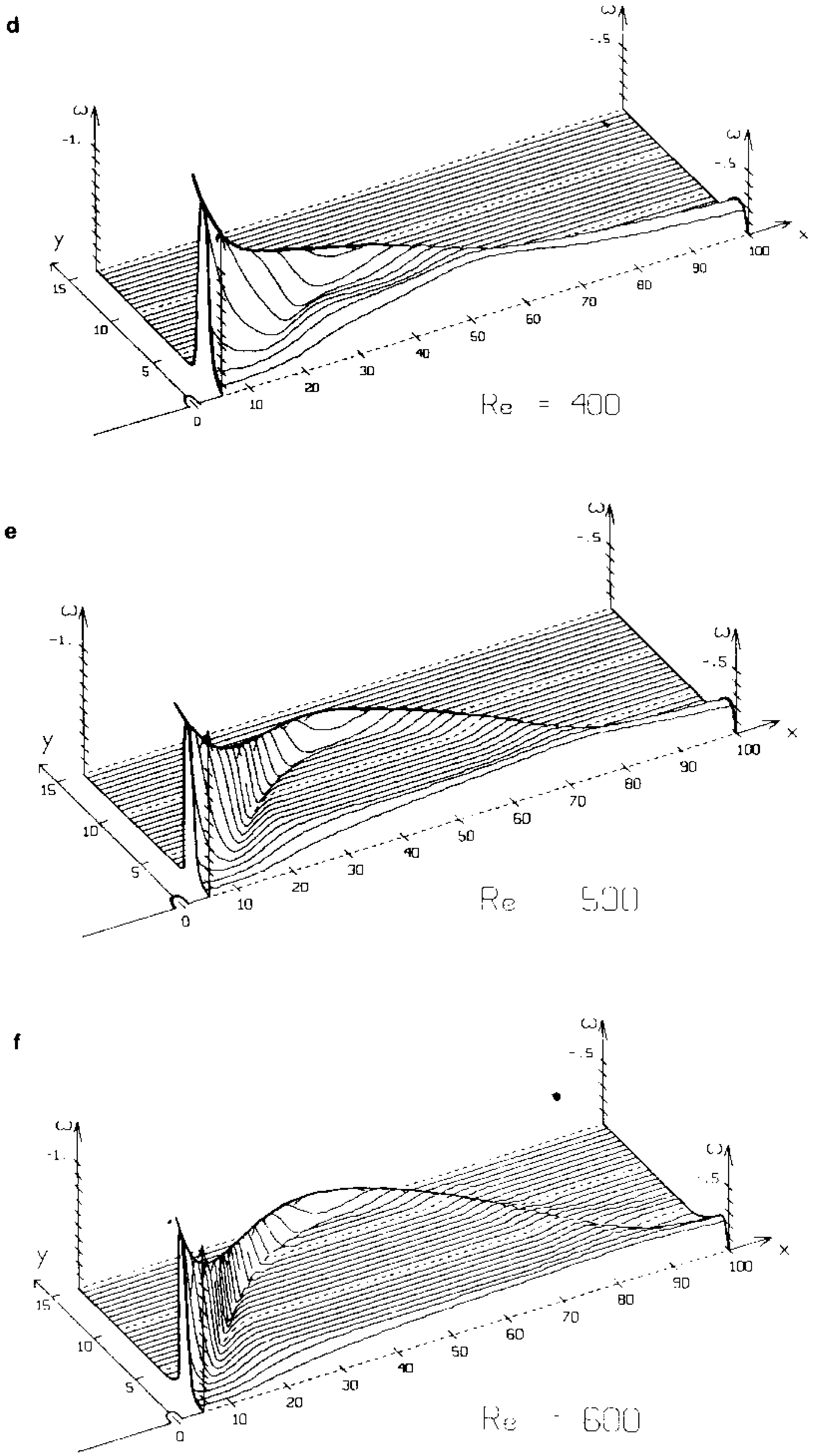

FIG. 9. Distribution of vorticity in wake behind cylinder.

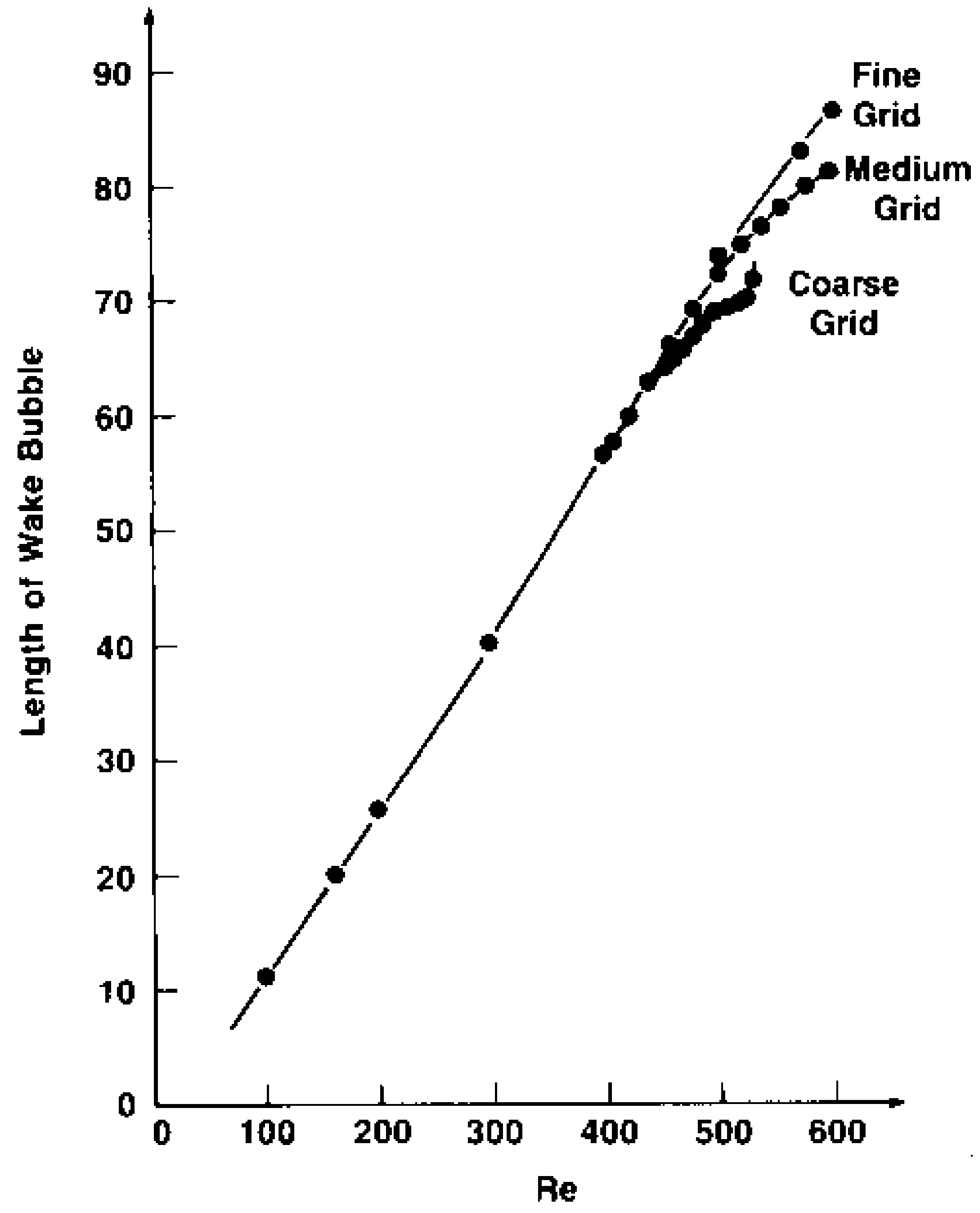

FIG. 10. Length of wake bubble (measured from the center of the cylinder).

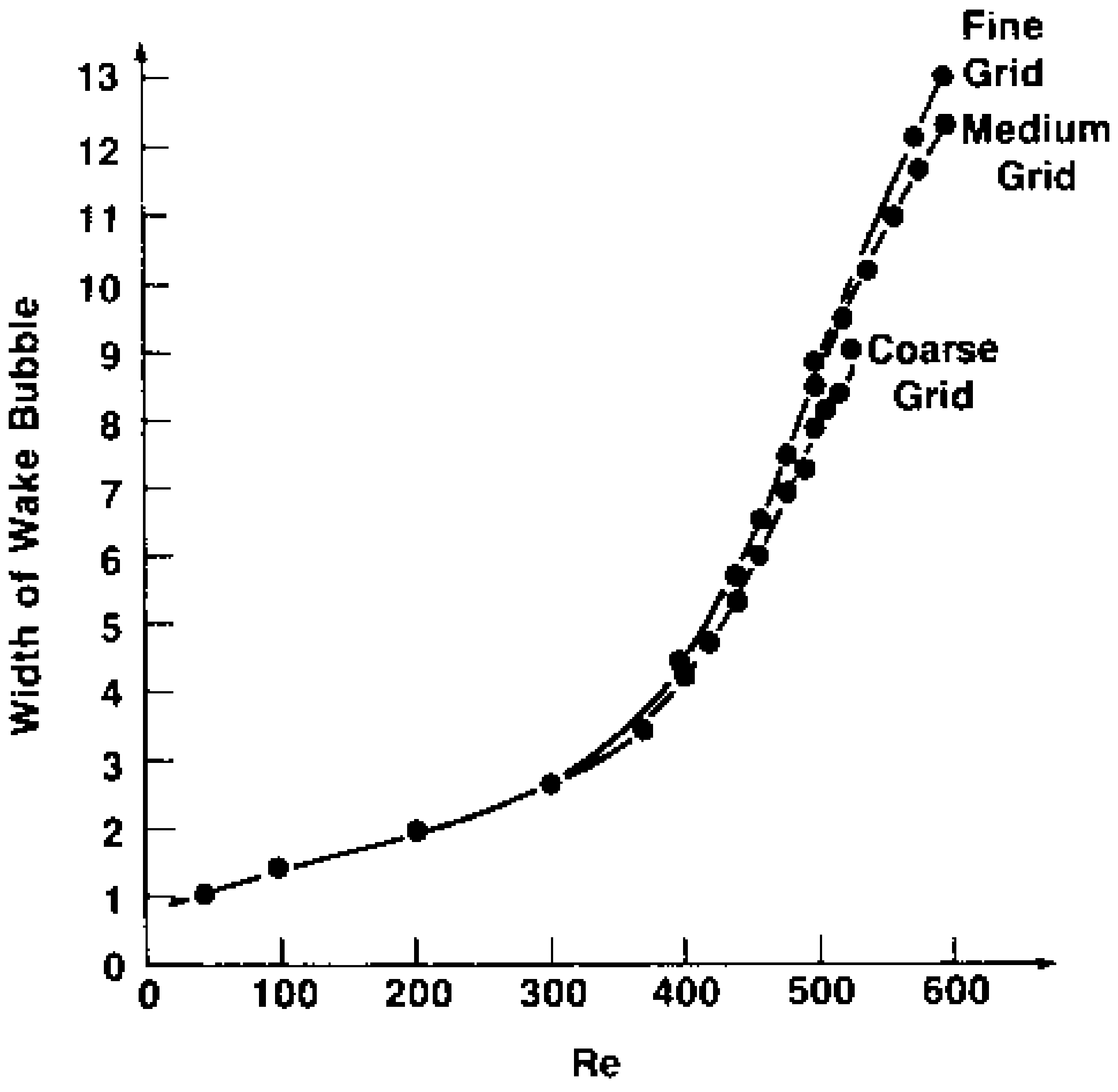

FIG. 11. Width of the wake bubble.

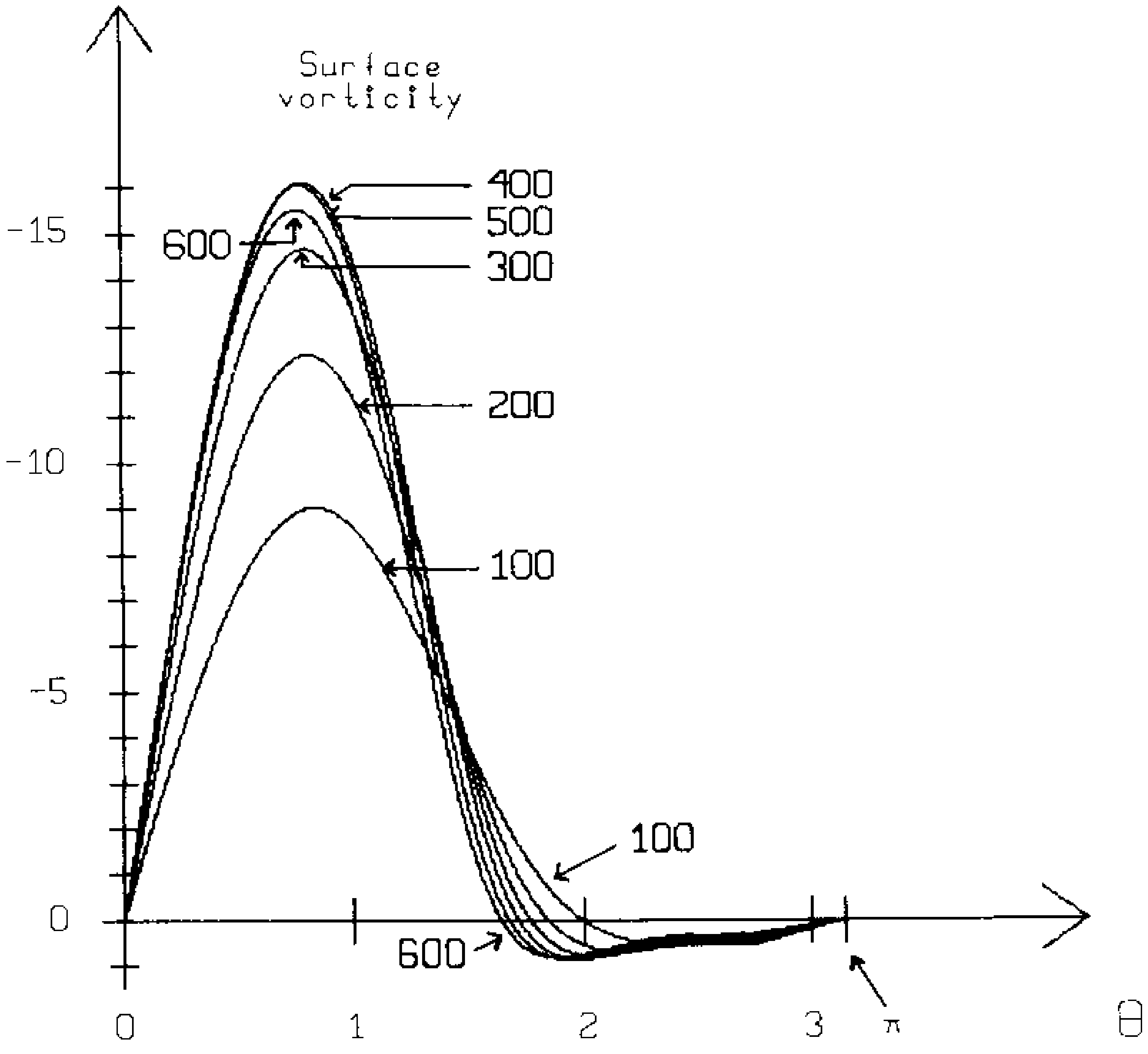

FIG. 12. Vorticity on the body surface.

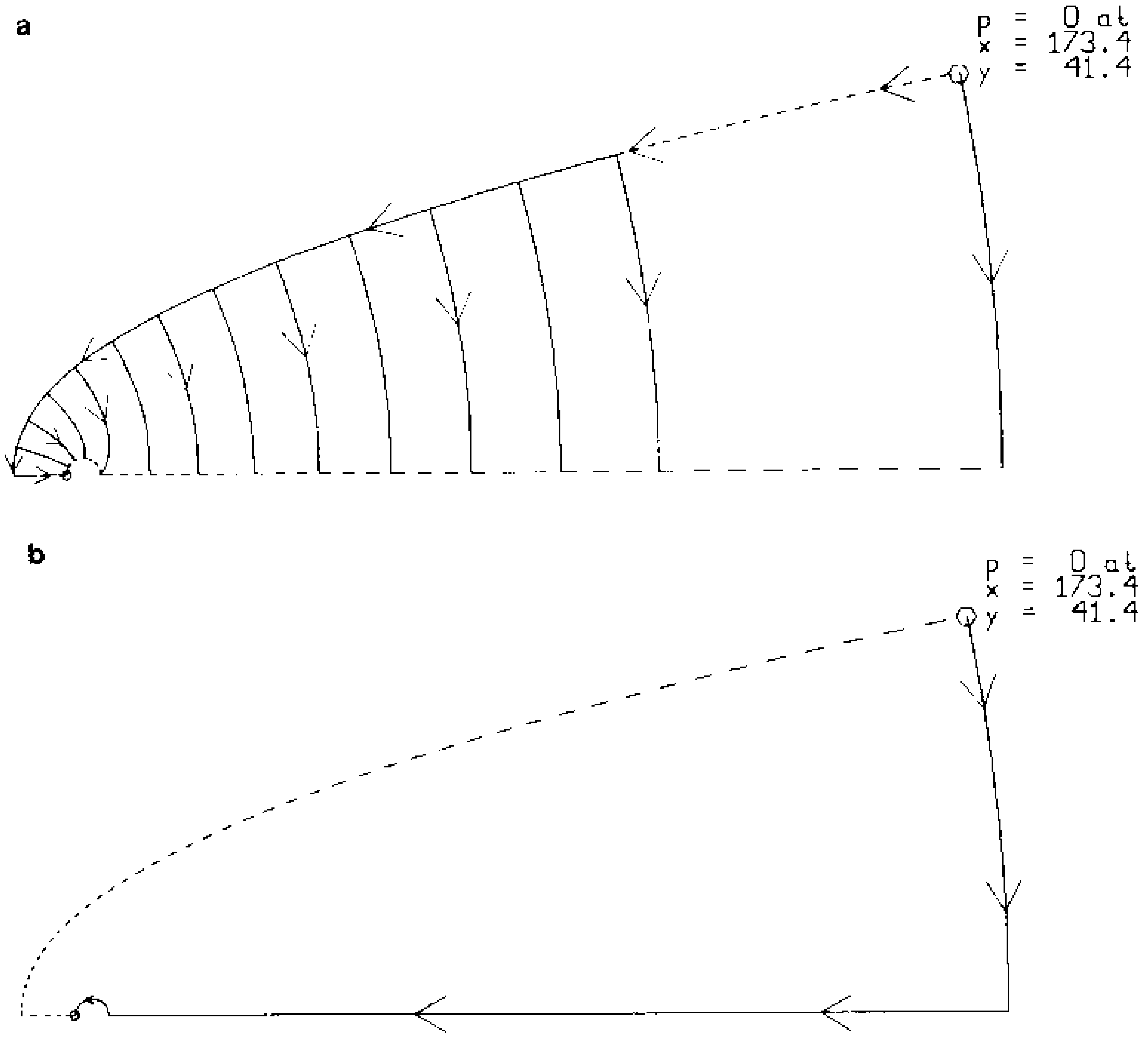

FIG. 13. (a) Integration paths for the pressure field; (b) integration path for accuracy verification.

TABLE I

Front Stagnation Pressure as Function of Integration Path

Reynolds number	Front stagnation pressure following path in Figures 13a	13b
100	0.5304	0.5325
200	0.5150	0.5170
300	0.5091	0.5109
400	0.5043	0.5057
500	0.4963	0.4971
600	0.4871	0.4873

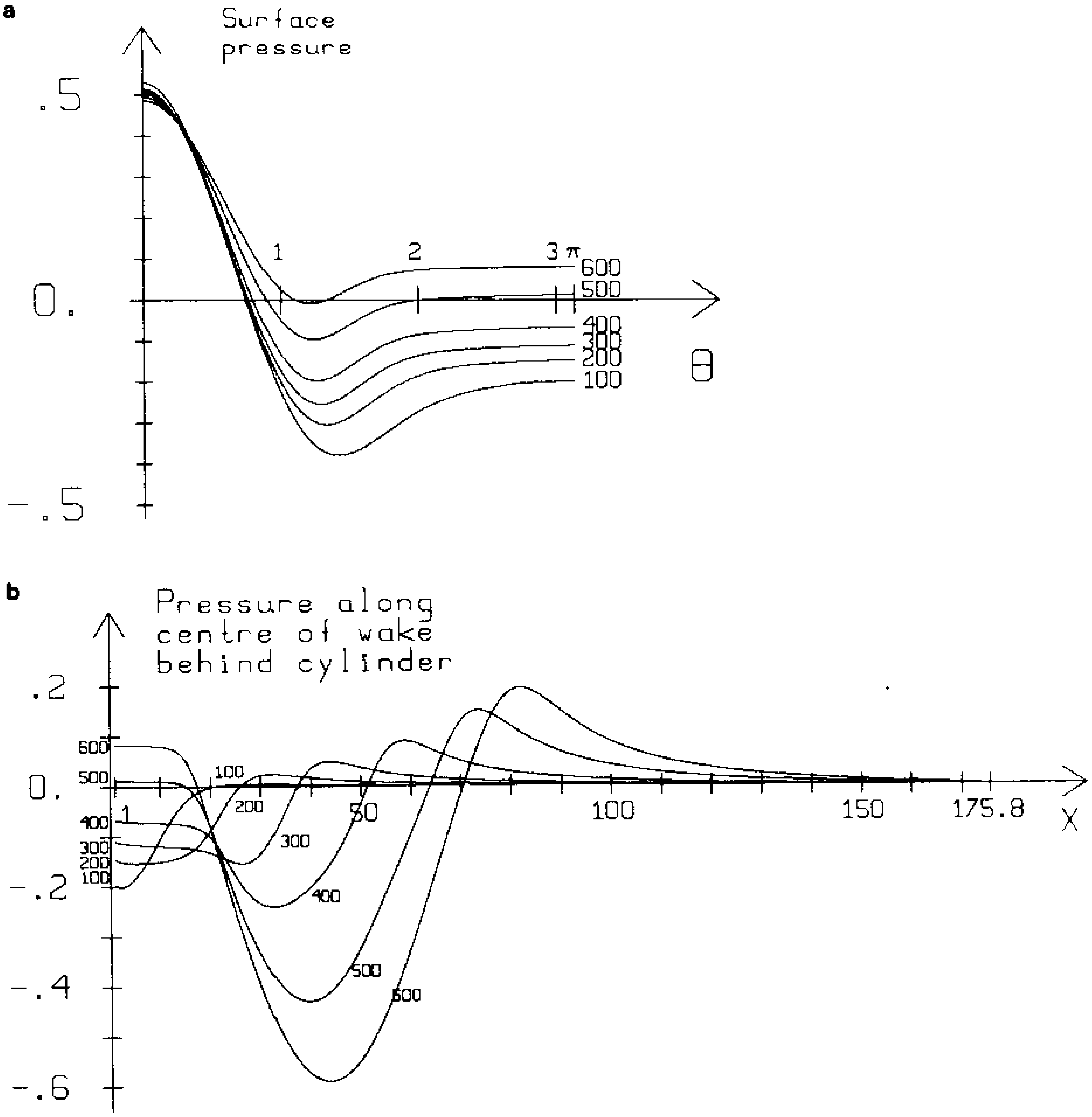

FIG. 14. (a) Pressure on the body surface; (b) pressure along the centre of the wake.

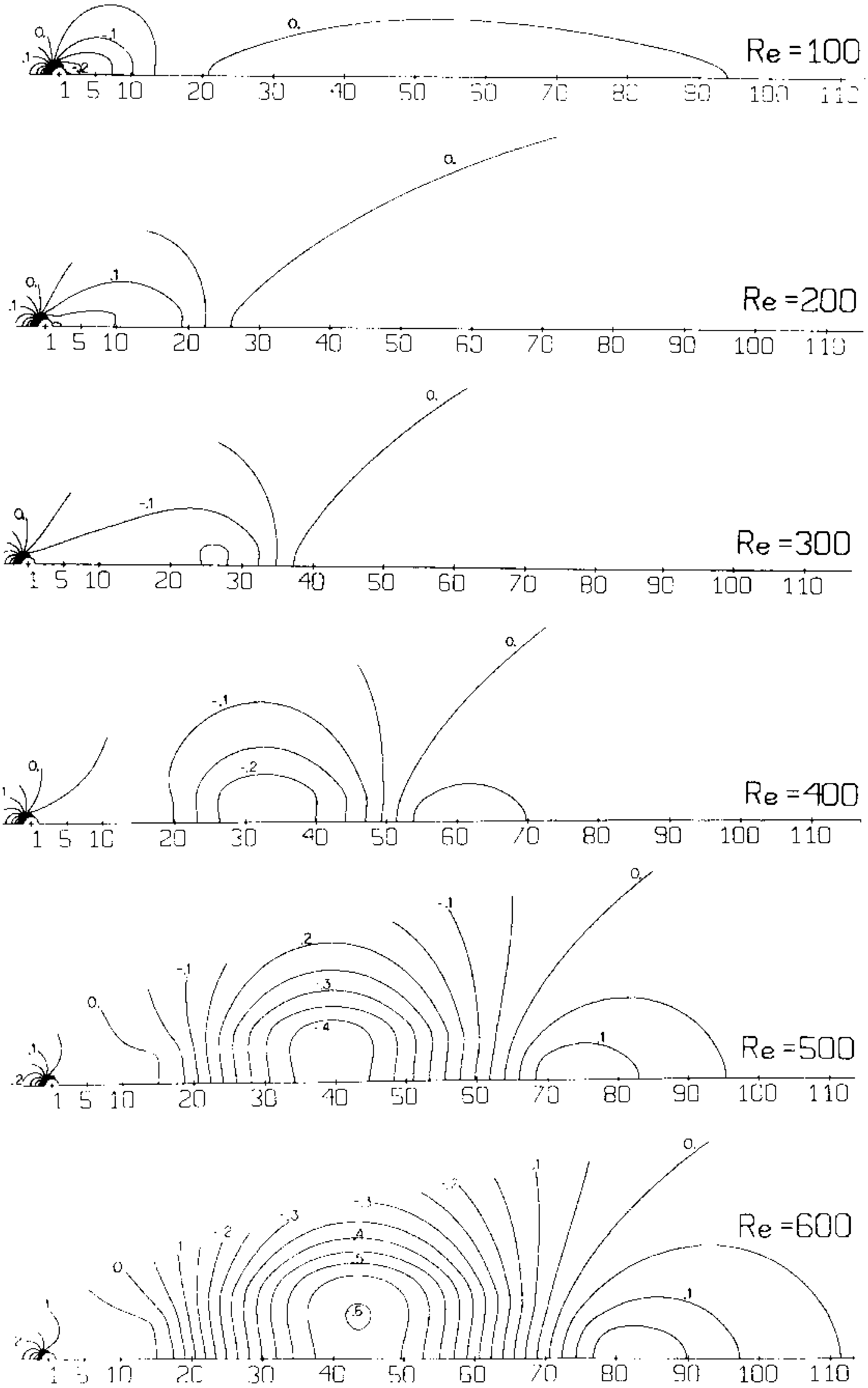

FIG. 15. Pressure fields.

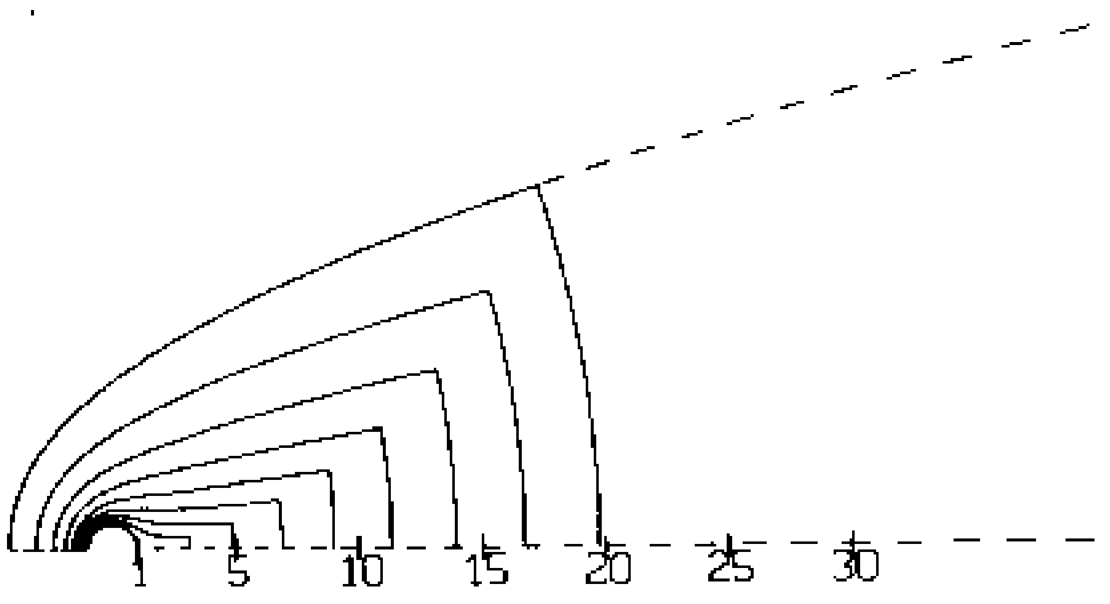

FIG. 16. Integration paths for calculation of the drag coefficient.

Table I compares the front stagnation pressure following these two paths in order to demonstrate the accuracy in the integration of (16) and (17). However, our normalization causes this pressure to fall slightly below 0.5 in conflict with theoretical results (e.g., in [7]).

Figures 14a and b show the pressure along the body surface and along the line of symmetry behind the body. Complete pressure fields are shown in Figs. 15a–e.

The drag coefficient C_D can be calculated as a line integral around the body. For a path Γ enclosing the cylinder in the physical x plane, the generalized Blasius formula (see, e.g., [9]) gives

$$C_D = -\mathrm{Re}\left\{2i\oint_\Gamma \left(\frac{\partial\Psi}{\partial x}\right)^2 dx + i\oint_\Gamma \omega\bar{x}\,d\Psi + \frac{4}{\mathrm{Re}}\oint_\Gamma \frac{\partial\omega}{\partial\bar{x}}\,\bar{x}\,d\bar{x}\right\}. \tag{18}$$

Expressed in a coordinate system $z = z(x)$, where $z(x)$ analytic, (18) becomes

$$C_D = -\mathrm{Re}\left\{2i\oint_{\Gamma'} \left(\frac{\partial\Psi}{\partial z}\right)^2 \frac{dz}{dx}\,dz + i\oint_{\Gamma'} \omega\bar{x}\,d\Psi + \frac{4}{\mathrm{Re}}\oint_{\Gamma'} \frac{\partial\omega}{\partial\bar{z}}\,x\,d\bar{z}\right\} \tag{19}$$

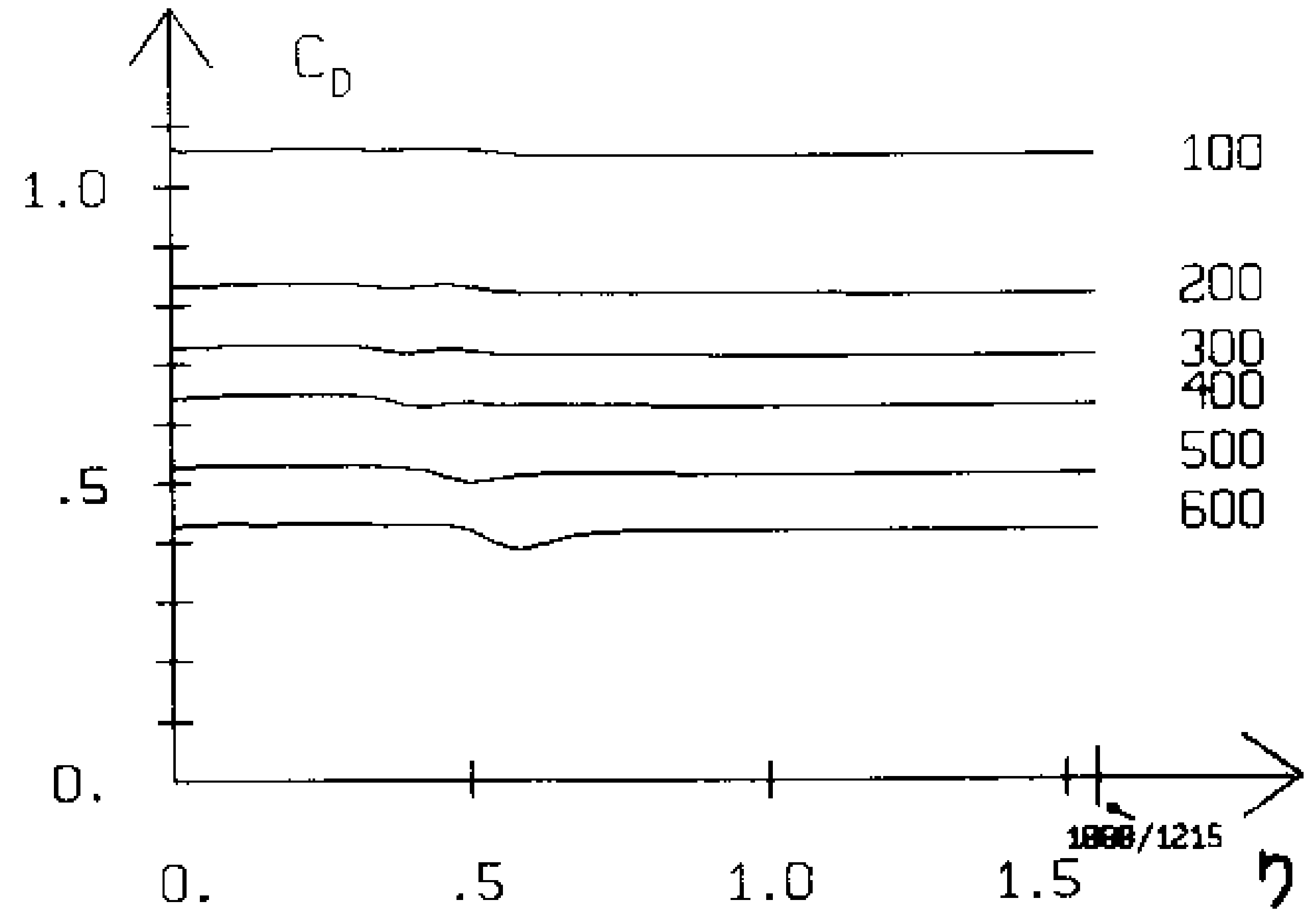

FIG. 17. Drag coefficient as function of the integration path.

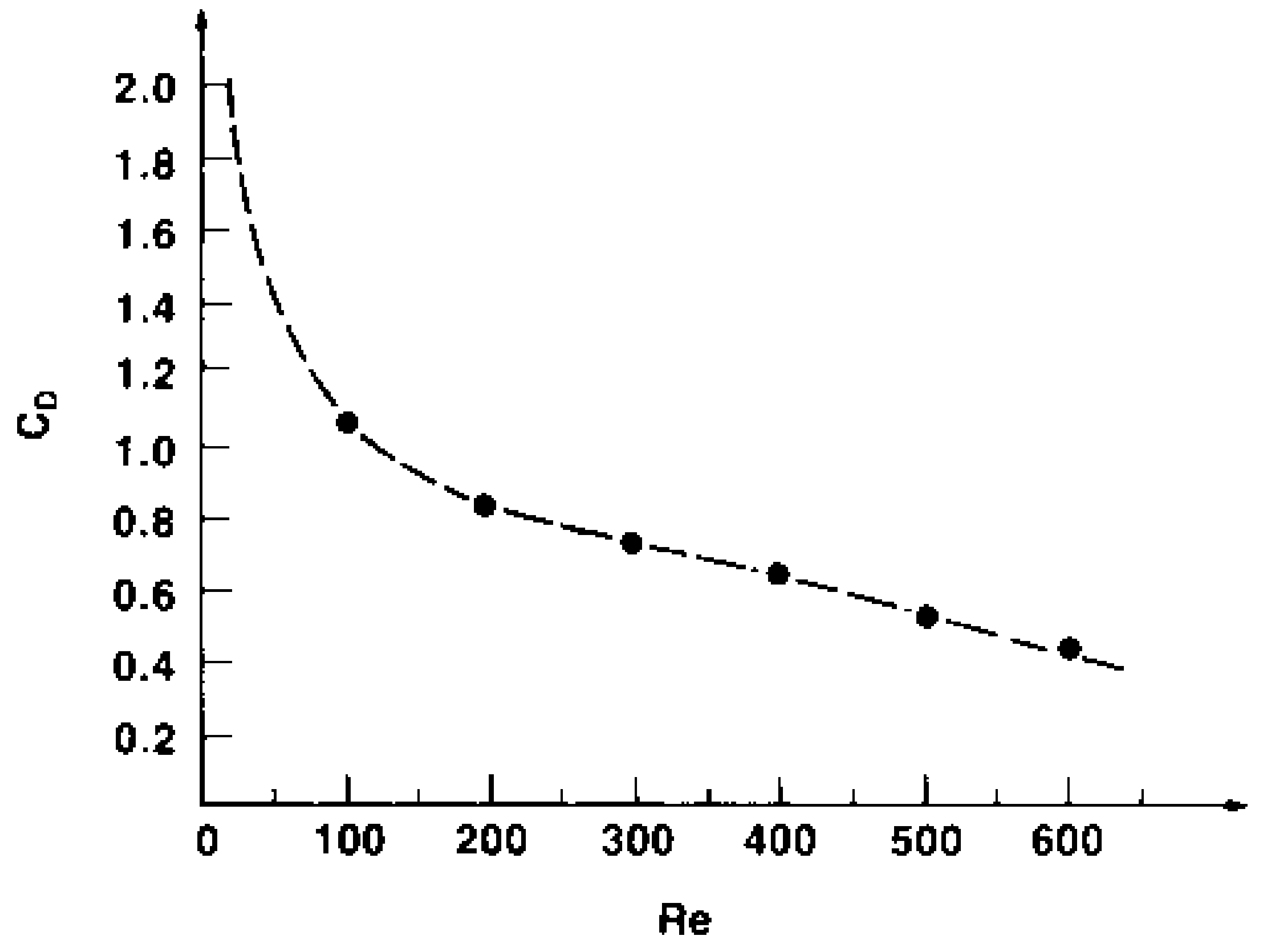

FIG. 18. Drag coefficient as function of the Reynolds number.

(with the conventional notations $z=\xi+i\eta$, $\bar{z}=\xi-i\eta$, $\partial/\partial z=\frac{1}{2}(\partial/\partial\xi-i\,\partial/\partial\eta)$, $\partial/\partial\bar{z}=\frac{1}{2}(\partial/\partial\xi+i\,\partial/\partial\eta)$).

Figure 16 shows the sequence of integration paths that were used and Fig. 17 the evaluated drag coefficients as functions of these paths (by the midpoint rule, Richardson extrapolated to fourth-order of accuracy). When the integration path follows the vortex sheet for some distance, integration errors build up. For paths either nearer or further away from the cylinder, C_D is found to be virtually independent of the choice of path. Figure 18 shows the drag coefficient as function of the Reynolds number and Table II compares these values for C_D with those reported in [6].

TABLE II

Drag Coefficient as Function of Re

Reynolds number	C_D	C_D according to [6]
100	1.060	1.058
200	0.833	0.829
300	0.729	0.722
400	0.645	—
500	0.528	—
600	0.430	—

TESTS OF ACCURACY

Three sources of errors are present:

1. rounding errors;
2. implementation of top and far right boundary conditions at finite distances; and
3. truncation errors because of finite differencing of derivatives.

The first source of errors proves to be negligible with the 64-bit floating point wordlength (48-bit mantissa).

The size of the second type of errors can be tested by moving the boundary in question in and out and checking how this influences quantities like wake length

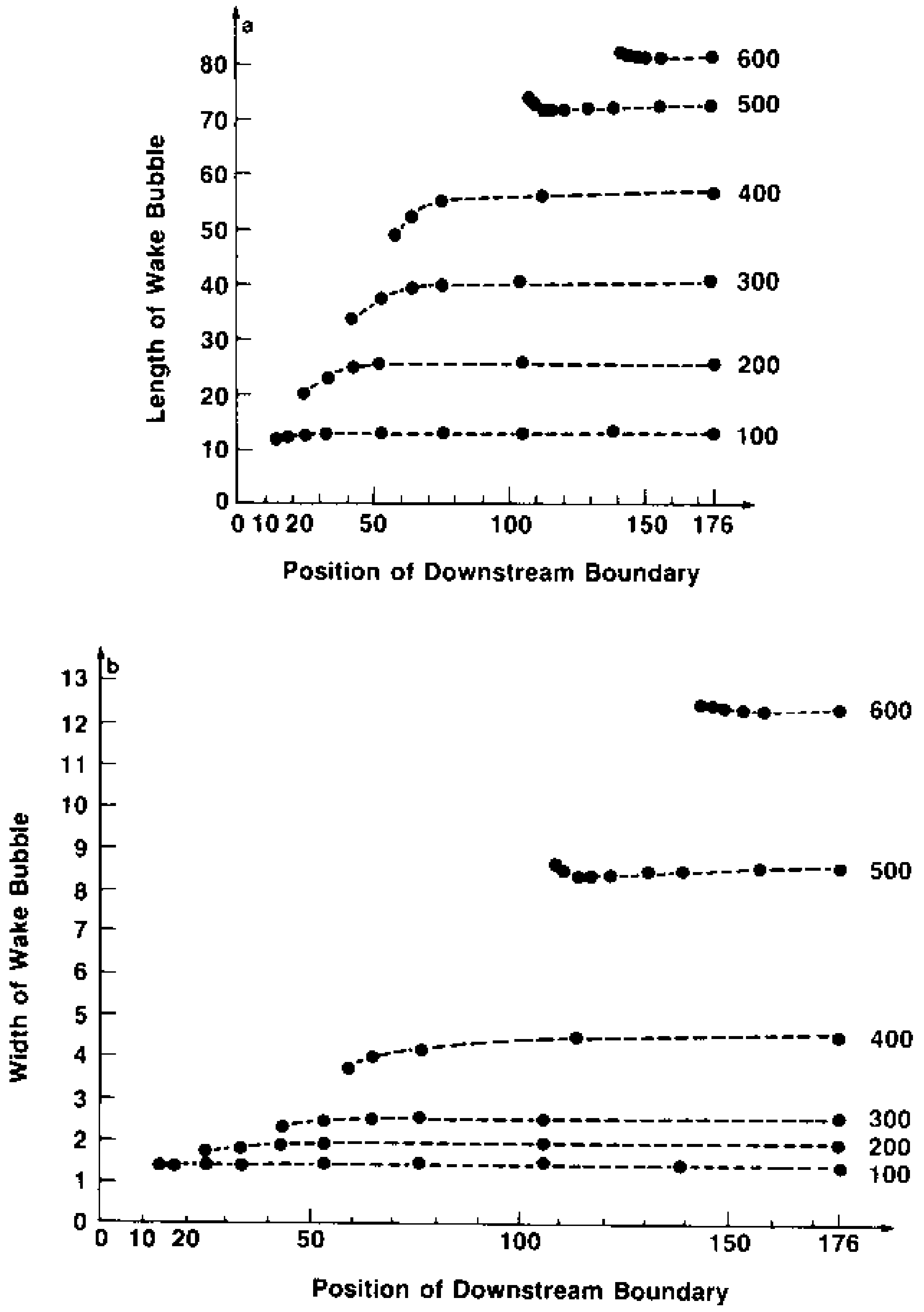

FIG. 19. Length (a) and width (b) of the wake bubble as a function of the position of the downstream boundary.

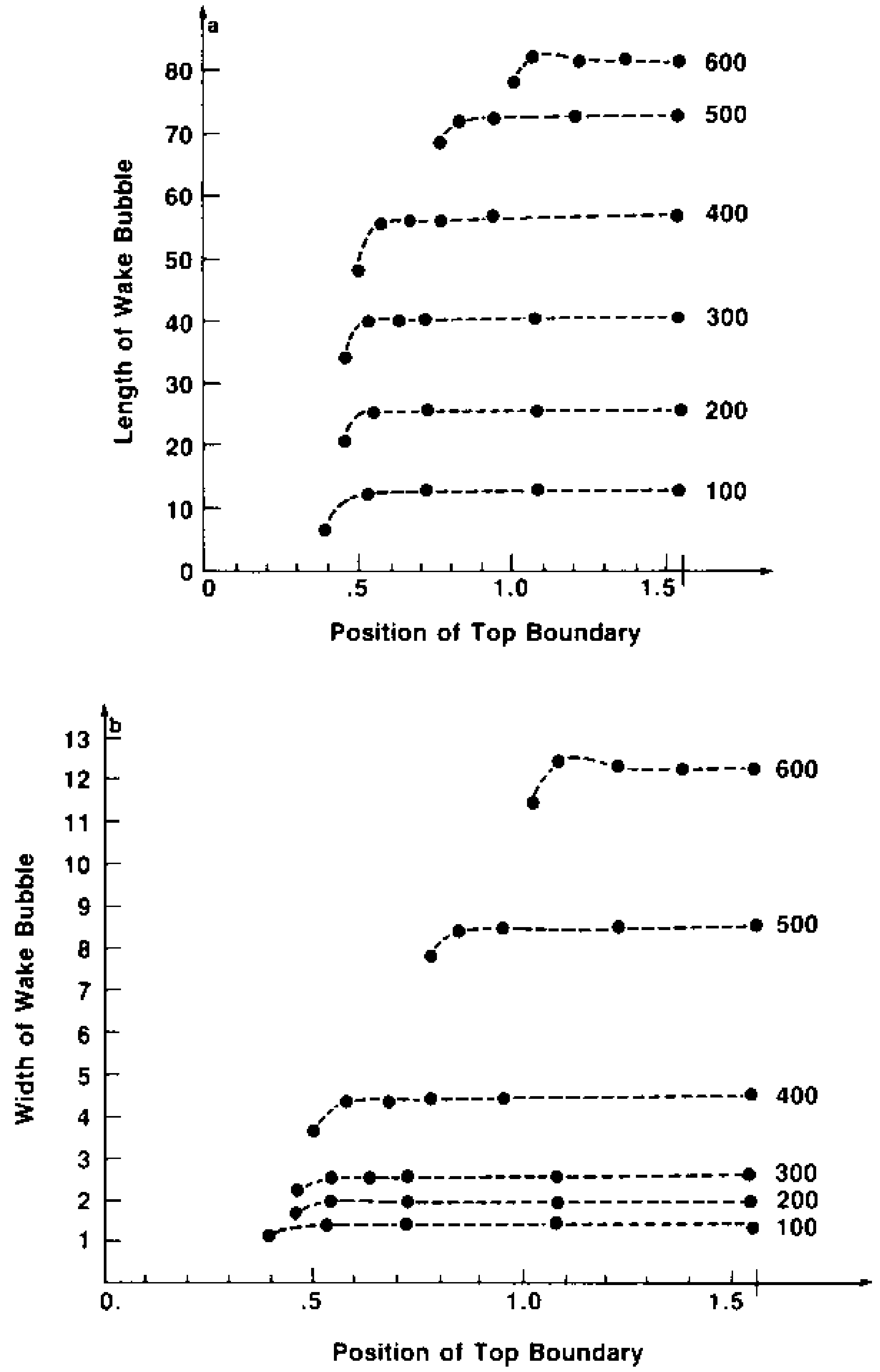

FIG. 20. Length (a) and width (b) of the wake bubble as a function of the position of the top boundary.

and width. Figures 19 and 20 show the results of these tests (for the top boundary condition in Fig. 20, compare with Fig. 2 to relate the η-value to the top boundary position).

The third source of errors, truncation errors in the difference approximations, is by far the most serious one. We displayed the discrepancies between different grid densities already in Figs. 10 and 11. Each coarser grid has $\frac{3}{2}$ times the step size in each direction compared to the nearest finer grid. With second-order accuracy, this translates into an increase in expected errors by a factor of $\frac{9}{4} \approx 2$ (the coarsest grid could be used only up to around $\mathrm{Re} = 530$ due to the emergence of a spurious turning point). Considering the way in which the coarser grids lose their accuracies for increasing values of Re, we are inclined to believe that the fine grid slightly underestimates the wake length and width at Re = 600. It seems likely that both length and width should be growing linearly with Re at this upper end of our calculation.

CONCLUSIONS

Apart from a few, very inaccurate calculations, Re = 120 is the highest Reynolds number reached by other investigators. Since we in [6] gave results up to Re = 300 and compared extensively with previous references, we have here limited ourselves to only a few comparisons with results in [6]. In most respects there is good agreement. The exception is that we now find the shortening (but not the widening) of the wake bubble near Re = 300 in [6] to have been erroneous.

This work falls short of establishing a limit process for Re → ∞. However, it seems quite clear that attempts to describe the wake at high Reynolds numbers should take note of the similarity between the main part of the wake bubble and translating regions of piecewise uniform vorticity. Regions of this kind are described for example in [13, 16, 21] and (with a vortex sheet at the edge) in [15, 20].

REFERENCES

1. D. N. DE G. ALLEN AND R. V. SOUTHWELL, *Q. J. Mech. Appl. Math.* **8** (1955), 129.
2. G. K. BATCHELOR, *J. Fluid Mech.* **1** (1956), 388.
3. S. BRODETSKY, *Proc. R. Soc. A* **102** (1923), 542.
4. S. C. R. DENNIS, *in* "Lecture Notes in Physics" (A. I. van de Vooren and P. J. Zandbergen, Eds.), Vol. 59, p. 165, Springer-Verlag, Berlin, 1976.
5. G. J. FIX AND S. P. MARIN, *J. Comput. Phys.* **28** (1978), 253.
6. B. FORNBERG, *J. Fluid Mech.* **98** (1980), 819.
7. A. S. GROVE, F. H. SHAIR, E. E. PETERSEN, AND A. ACRIVOS, *J. Fluid Mech.* **19** (1964), 60.
8. T. M. HAGSTROM AND H. B. KELLER, The numerical solution of semi-linear elliptic problems in unbound cylindrical domains, to appear in *SIAM J. Num. Analysis.*
9. I. IMAI, *Proc. R. Soc. A* **208** (1951), 487.
10. H. B. KELLER, *SIAM J. Sci. Statist. Comput.* **4** (1983), 573.
11. M. LENTINI AND H. B. KELLER, *SIAM J. Numer. Anal.* **17** (1980), 577.
12. D. H. PEREGRINE, *J. Fluid Mech.* **157** (1985), 493.
    of Mathematics, University of Bristol, 1981.
13. R. T. PIERREHUMBERT, *J. Fluid Mech.* **99** (1980), 129.
14. P. J. ROACHE, "Computational Fluid Dynamics," Hermosa, Albuquerque, N.M., 1976.
15. V. S. SADOVSKII, *Appl. Math. Mech.* **35** (1971), 729.
16. P. G. SAFFMAN AND S. TANVEER, *Phys. Fluids* **25** (1982), 1929.
17. P. G. SAFFMAN AND S. TANVEER, *J. Fluid Mech.* **143** (1984), 351.
18. F. T. SMITH, *J. Fluid Mech.* **92** (1979), 171.
19. F. T. SMITH, *J. Fluid Mech.* **113** (1981), 407.
20. F. T. SMITH, *J. Fluid Mech.* **155** (1985), 175.
21. H. M. WU, E. A. OVERMAN, II, AND N. J. ZABUSKY, *J. Comput. Phys.* **53** (1984), 42.

Printed by the St. Catherine Press Ltd., Tempelhof 41, Bruges, Belgium